

**Evolution from spherical single-particle structure to stable triaxiality at high spins in  $^{140}\text{Nd}$** 

C. M. Petrache,<sup>1</sup> M. Fantuzzi,<sup>1</sup> G. LoBianco,<sup>1</sup> D. Mengoni,<sup>1</sup> A. Neusser-Neffgen,<sup>2</sup> H. Hübel,<sup>2</sup> A. Al-Khatib,<sup>2</sup> P. Bringel,<sup>2</sup> A. Bürger,<sup>2</sup> N. Nenoff,<sup>2</sup> G. Schönwasser,<sup>2</sup> A. K. Singh,<sup>2,\*</sup> I. Ragnarsson,<sup>3</sup> G. B. Hagemann,<sup>4</sup> B. Herskind,<sup>4</sup> D. R. Jensen,<sup>4</sup> G. Sletten,<sup>4</sup> P. Fallon,<sup>5</sup> A. Gørgen,<sup>5,†</sup> P. Bednarczyk,<sup>6,7,‡</sup> D. Curien,<sup>6</sup> G. Gangopadhyay,<sup>8</sup> A. Korichi,<sup>9</sup> A. Lopez-Martens,<sup>9</sup> B. V. T. Rao,<sup>10</sup> T. S. Reddy,<sup>10</sup> and Nirmal Singh<sup>11</sup>

<sup>1</sup>*Dipartimento di Fisica, Università di Camerino and Istituto Nazionale di Fisica Nucleare, Sezione di Perugia, I-62032, Camerino, Italy*

<sup>2</sup>*Helmholtz-Institut für Strahlen- und Kernphysik, Universität Bonn, Nußallee 14-16, D-53115 Bonn, Germany*

<sup>3</sup>*Department of Mathematical Physics, Lund Institute of Technology, S-22362 Lund, Sweden*

<sup>4</sup>*Niels Bohr Institute, Blegdamsvej 17, DK-2100 Copenhagen, Denmark*

<sup>5</sup>*Nuclear Science Division, Lawrence Berkeley National Laboratory, Berkeley, California 94720, USA*

<sup>6</sup>*Institut de Recherches Subatomiques, 23 Rue du Loess, F-67037 Strasbourg, France*

<sup>7</sup>*The Niewodniczanski Institute of Nuclear Physics, Polish Academy of Sciences, ulitsa Radzikowskiego 152, PL-31342 Krakow, Poland*

<sup>8</sup>*Department of Physics, University College of Science, 92 A.P.C. Road, Kolkata 700009, India*

<sup>9</sup>*Centre de Spectrometrie Nucleaire et de Spectrometrie de Masse, F-91405 Orsay Campus, France*

<sup>10</sup>*Department of Nuclear Physics, Andhra University, Visakhapatnam 530003, India*

<sup>11</sup>*Department of Physics, Panjab University, Chandigarh 160014, India*

(Received 24 May 2005; published 22 December 2005)

The level structure of  $^{140}\text{Nd}_{80}$  has been established up to spin 48 by in-beam  $\gamma$ -ray spectroscopy by use of the  $^{96}\text{Zr}(^{48}\text{Ca}, 4n)$  reaction. High-fold  $\gamma$ -ray coincidences were measured with the EUROBALL spectrometer. Twelve new rotational bands have been discovered at high spins. They are interpreted as being formed in a deep triaxial minimum at  $\varepsilon_2 \approx 0.25$  and  $\gamma \approx 35^\circ$ . Possible configurations are assigned to the observed bands on the basis of configuration-dependent cranked Nilsson-Strutinsky calculations.

DOI: [10.1103/PhysRevC.72.064318](https://doi.org/10.1103/PhysRevC.72.064318)

PACS number(s): 21.10.Re, 21.60.Ev, 23.20.Lv, 27.60.+j

## I. INTRODUCTION

The existence of stable triaxiality in nuclei has been intensively investigated in recent years, both theoretically and experimentally. Triaxiality is difficult to prove experimentally. Several observations that have been explained by deviations from axial symmetry, like signature splitting and signature inversion or the measured transition probabilities, may also be interpreted in different ways. However, two phenomena that are uniquely related to triaxiality have been predicted theoretically [1,2]: the occurrence of wobbling and chiral bands. In the  $A = 165$  mass region, wobbling was observed [3], indicating that the corresponding bands are triaxial, and in the  $A = 130$  region energetically degenerate bands might be evidence for chiral bands [4,5]. It is also evident that triaxiality plays a key role in terminating bands, and it is now well established that such bands [6,7] identified, e.g., in the  $A = 60$ ,  $A = 110$ , and  $A = 150$  regions must traverse the triaxial plane on their way from high collectivity at low-spin values to the noncollective terminating state. Triaxiality in the mass  $A = 130$  region was predicted more than 30 years ago [8], and more recent total-potential-energy calculations performed either with the configuration-dependent cranked

Nilsson-Strutinsky (CNS) model [9] or with the ultimate cranked code [10,11] show well-developed local minima with large triaxiality with which the observed wobbling and chiral bands are associated. Thus these observations give confidence in the calculated potential-energy surfaces (PESs).

In the  $A = 130$ – $150$  region, PES calculations predict a variety of minima corresponding to spherical or near-spherical, low-deformation oblate or prolate, triaxial, and superdeformed (SD) shapes. A large number of rotational bands that can be associated with SD [12] and other different minima have previously been found [13]. The predicted shape coexistence has been confirmed by lifetime measurements from which quadrupole moments have been deduced. The bands that show small quadrupole moments  $Q_T \sim 2$ – $4 eb$  and relatively small moments of inertia ( $\sim 50 \hbar^2 \text{MeV}^{-1}$ ) have been associated with low-deformation and/or triaxial PES minima with  $\gamma \approx -80^\circ$  [14] or  $\gamma \approx -30^\circ$  [15]. The recently discovered bands in  $^{138,139}\text{Nd}$ , which show a very low dynamic moment of inertia  $J^{(2)} \sim 20 \hbar^2 \text{MeV}^{-1}$ , have been consistently interpreted as triaxial structures with  $\gamma \approx +35^\circ$  [16]. At the lower end of the mass region, near  $A = 130$ , the second well has a moderate deformation ( $\varepsilon_2 \approx 0.3$ – $0.4$ ); see, e.g., the deduced quadrupole moments for the highly deformed bands of Nd and Ce nuclei in Refs. [17–19]. The deformation of the second well is then increasing with increasing mass, reaching  $\varepsilon \approx 0.45$  in the recently discovered SD band in  $^{140}\text{Nd}$  [20] and coming close to  $\varepsilon \approx 0.6$  (corresponding to a nuclear axis ratio of 2:1) at the upper end near  $A = 150$ ; see, e.g., the quadrupole moments deduced for the SD bands of Dy and Gd nuclei in Refs. [21–24].

In this work we report on results of a detailed study of the level structure of  $^{140}\text{Nd}$  up to spin 48. Previously, only

\*Present address: Department of Physics, IIT Kharagpur, Kharagpur-721302, India.

†Present address: DAPNIA/SPhN, CEA Saclay, F-91191 Gif-sur-Yvette, France.

‡Present address: Gesellschaft für Schwerionenforschung, Planckstrasse, 1, D-64291 Darmstadt, Germany.

spherical or near-spherical states up to spin 17 were known in this nucleus [25]. In Secs. II and III the experimental details and results that lead to the construction of the extended level scheme are presented. In Sec. IV the level structure of  $^{140}\text{Nd}$  is discussed, followed by a short summary in Sec. V.

## II. EXPERIMENTAL DETAILS

High-spin states in  $^{140}\text{Nd}$  have been populated in the reaction  $^{96}\text{Zr}(^{48}\text{Ca},4n)$  with a 195-MeV  $^{48}\text{Ca}$  beam delivered by the Vivitron tandem accelerator at the Institut de Recherches Subatomiques, Strasbourg. A self-supporting  $^{96}\text{Zr}$  foil of  $735\text{-}\mu\text{g}/\text{cm}^2$  thickness was used as a target. Gamma-ray coincidences were measured with the EUROBALL spectrometer [26], consisting of 30 single, tapered Ge detectors and 15 cluster and 26 clover composite Ge detectors, each surrounded by a  $\text{Bi}_4\text{Ge}_3\text{O}_{12}$  (BGO) Compton-suppression shield. Out of the total number of 239 Ge crystals, 230 could be used in our analysis. Multiplicity information was obtained from the “inner ball” of 210 BGO detectors. Events were written to tape with the requirement that at least 11 BGO detectors of the inner ball and four Ge crystals before Compton suppression were in prompt coincidence. Presorting of the data, which included Compton suppression and add-back for the composite detectors, resulted in a total of  $1.5 \times 10^9$  events with a  $\gamma$ -ray coincidence fold of  $f \geq 3$ .

The  $\gamma$ -ray coincidences were sorted into three- and four-dimensional coincidence arrays (cube and hypercube, respectively), and the analysis was carried out with the RADWARE software package [27]. To determine the multipolarity of transitions, several gated matrices (with gates set on all detectors on specific transitions with known quadrupole and dipole character of  $^{140}\text{Nd}$ ) were sorted with all detectors on one axis and detectors at  $90^\circ$  and at forward/backward (f,b) angles, respectively, on the other axis. Gates were set on the axis with all detectors, and the intensity ratio  $W(\text{f,b})/W(90^\circ)$ , which we denote as  $R_{\text{DCO}}$  (DCO means Directional Correlation from Oriented States), was determined for the transitions in the resulting spectra. The multipolarity of the new transitions identified in  $^{140}\text{Nd}$  were assigned based on the comparison of the deduced  $R_{\text{DCO}}$  ratios with the average  $R_{\text{DCO}}$  ratios extracted for known pure  $E2$  and  $E1$  transitions in nuclei populated in the reaction, which are  $1.09 \pm 0.02$  and  $0.64 \pm 0.01$ , respectively.

## III. RESULTS AND LEVEL SCHEME

In this section the results obtained in our experiment for  $^{140}\text{Nd}$  are presented. The level scheme resulting from the present analysis is shown in Figs. 1 and 2. The most recent previous study of the level scheme dates back to 1987 [25]. In that work the level structure was established up to spin 17. Three isomers were previously identified with lifetimes between 0.25 ns and 0.6 ms. They are the  $7^-$  state at 2221 keV with 0.6 ms [28], the  $10^+$  level at 3619 keV with 32(1) ns [25,29], and possibly an  $I = 12$  isomer at 4512 keV with 0.25 ns [30].

Our analysis revealed a number of high-spin bands, extending the level scheme up to spin 48. Examples of the  $\gamma$ -ray

coincidence spectra for the new bands are displayed in Fig. 3. The in-band transitions have energies that increase regularly by about 150–250 keV at each step, except at the bottom and/or the top of the cascades, where irregularities that are due to interactions with other structures are present.

The spectroscopic information on the  $\gamma$ -ray transitions of the bands connected to low-lying states is given in Table I, whereas the information on the floating bands is given in Table II.

The results of the present study confirm the main features of the level scheme published previously [25]. First, we clearly see the low-energy 90-keV transition between the  $6^+$  and  $5^-$  states. We also confirm the transitions deexciting the  $7_2^-$ ,  $8^-$ , and  $9^-$  states. Above the  $9^-$  state, as already observed previously [25], the main decay flux proceeds by means of two cascades: one consisting of the 867.8-, 190.9-, 188.5-, 728.1-keV [ $R_{\text{DCO}} = 0.66(2)$ ], 211.8-keV [ $R_{\text{DCO}} = 0.59(3)$ ], 258.4-keV [ $R_{\text{DCO}} = 0.57(7)$ ] and 505.3-keV [ $R_{\text{DCO}} = 0.55(8)$ ] transitions, and another consisting of the 720.3-, 922.4-keV [ $R_{\text{DCO}} = 1.04(5)$ ], and 212.9-, 119.7-, 181.6-, and 544.3-keV [ $R_{\text{DCO}} = 0.46(2)$ ] transitions. We confirm the first cascade, and in parallel to it we also observe the new weak transitions of 791.2 keV ( $10^- \rightarrow 8^-$ ), 608.2 keV ( $13^- \rightarrow 13^-$ ), and 437.3 keV ( $17^- \rightarrow 15^-$ ). The 439.8-keV transition reported in Ref. [25] was not observed. The highest previously observed  $17^-$  level on this branch at 6403.7 keV is populated by several high-energy transitions {1116.6 keV [ $R_{\text{DCO}} = 0.66(10)$ ], 1404.1 keV [ $R_{\text{DCO}} = 0.57(16)$ ], 1416.0 keV [ $R_{\text{DCO}} = 0.71(11)$ ], and 1541.1 keV} deexciting states with spin 18. In the same region of the level scheme we have also identified four new weak transitions, with energies of 312.7, 275.9 [ $R_{\text{DCO}} = 0.46(2)$ ], 329.8, and 447.4 keV, which are connected by the 605.8- and 674.2-keV transitions to the  $15^-$  and  $16^-$  states of the main cascade, respectively.

Special attention was paid to the spin-parity assignment. The parity of the  $I = 10$  and 11 states in this cascade at 4028.8 and 4320.7 keV, respectively, is negative, since the connecting 867.8- and 575.9-keV transitions to the lower-lying  $9^-$  state have  $E2$  character.

The parity of the next higher-energy level in this cascade with  $I = 12$  at 4511.6 keV (with a possible lifetime of 0.25 ns [30]) is essential for the determination of the parities of the higher-spin states. It decays by the 190.9- and 482.8-keV [ $R_{\text{DCO}} = 1.03(5)$ ] transitions to the  $11^-$  and  $10^-$  states, respectively, but not to the  $10^+$  isomer. The observation of a  $12 \rightarrow 10^-$  instead of a  $12 \rightarrow 10^+$  transition strongly suggests negative parity for the  $I = 12$  state, since  $E2$  multipolarity is more likely than  $M2$ . For the strong 190.9-keV transition a careful angular-distribution analysis was performed. If we assume a value of  $\sigma/I = 0.3$  for the orientation parameter, which is typical in heavy-ion reactions, and also assume that there is no significant feeding from isomeric states above the 4511.6-keV level, the experimental  $W(\text{f,b})/W(90^\circ)$  ratio of 0.68(2) is compatible with a mixed transition of about 97.5(1.5)% dipole and 2.5(1.5)% quadrupole. Therefore the 190.9-keV transition is most probably a mixed  $M1/E2$  transition, since for an  $E1$  transition one would expect no  $M2$  admixture. We have also calculated the  $W(\text{f,b})/W(90^\circ)$

TABLE I. Spectroscopic information for levels and  $\gamma$  rays of the new bands in  $^{140}\text{Nd}$  that are linked to low-lying states.

Band number (Relative intensity)	$E_i^{\text{level}}$ (keV)	$E_\gamma$ (keV) <sup>a</sup>	Transition intensities <sup>b</sup>	Anisotropy <sup>c</sup> $I_i^\pi \rightarrow I_f^\pi$	Assignment	Multipolarity
Band 1 (19%)	9166.6	734.2	6	0.57(4)	$21^- \rightarrow 20^-$	$M1/E2$
	9787.3	620.7	5.5	1.17(5)	$23^- \rightarrow 21^-$	$E2$
		527.3	8.2	0.64(3)	$23^- \rightarrow 22^-$	$M1/E2$
	10568.6	781.3	19.2	1.06(5)	$25^- \rightarrow 23^-$	$E2$
		449.5	4.4	0.59(6)	$25^- \rightarrow 24^-$	$M1/E2$
	11357.3	788.7	13.7	1.09(4)	$27^- \rightarrow 25^-$	$E2$
	12413.1	1055.8	9.6	1.02(6)	$29^- \rightarrow 27^-$	$E2$
	13693.6	1280.4	4.4	1.08(17)	$31^- \rightarrow 29^-$	$E2$
	15135.2	1441.6	0.8	1.04(12)	$33^- \rightarrow 31^-$	$E2$
Band 2 (20%)	7807.8	1653.7	9.6	1.25(11)	$18^- \rightarrow 16^-$	$E2$
		845.8	6.0	0.52(3)	$18^- \rightarrow 17^-$	$M1/E2$
		755.8	2.7	0.41(6)	$18^- \rightarrow 17^-$	$M1/E2$
		1404.1	1.9	0.57(16)	$18^- \rightarrow 17^-$	$M1/E2$
	8432.4	605.6	0.5		$18^- \rightarrow 18^-$	$M1/E2$
		624.6	20.5	1.00(4)	$20^- \rightarrow 18^-$	$E2$
	9260.0	612.7	2.7	1.08(22)	$20^- \rightarrow 18^-$	$E2$
		827.6	21.9	1.03(5)	$22^- \rightarrow 20^-$	$E2$
	10119.1	859.1	8.2	1.08(6)	$24^- \rightarrow 22^-$	$E2$
	11165.8	1046.7	6.3	1.16(21)	$26^- \rightarrow 24^-$	$E2$
	12436.4	1270.6	1.9		$(28^-) \rightarrow 26^-$	
	Band 3 (7%)	9562.8	533.6	4.1	0.44(2)	$22^{(+)} \rightarrow 21^{(+)}$
587.7			2.2		$22^{(+)} \rightarrow (21^+)$	
10300.3		737.5	6.8	1.11(5)	$24^{(+)} \rightarrow 22^{(+)}$	$E2$
11064.7		764.4	5.5	1.20(5)	$26^{(+)} \rightarrow 24^{(+)}$	$E2$
12115.7		1051.0	2.7	1.23(17)	$28^{(+)} \rightarrow 26^{(+)}$	$E2$
13396.8		1281.1	1.4		$(30^+) \rightarrow 28^{(+)}$	
14833.1		1436.3	0.5		$(32^+) \rightarrow (30^+)$	
Band 4 (4%)	11837.6	772.9	2.7	0.60(2)	$27^{(+)} \rightarrow 26^{(+)}$	$M1/E2$
		447.3	0.3		$27^{(+)} \rightarrow$	
	12516.6	679.0	3.6	1.13(5)	$29^{(+)} \rightarrow 27^{(+)}$	$E2$
		400.9	0.3		$29^{(+)} \rightarrow 28^{(+)}$	$M1/E2$
	13573.8	1057.2	4.1	1.07(7)	$31^{(+)} \rightarrow 29^{(+)}$	$E2$
	14893.3	1319.5	1.4	1.04(16)	$33^{(+)} \rightarrow 31^{(+)}$	$E2$
16331.6	1438.3	0.5		$(35^+) \rightarrow 33^{(+)}$		
Band 5 (2%)	12470.4	1113.1	0.05		$(29^-) \rightarrow 27^-$	
	13383.9	913.5	1.0		$31^- \rightarrow (29^-)$	
		970.8	0.8	1.03(20)	$31^- \rightarrow 29^-$	$E2$
	14461.7	992.0	0.5		$31^- \rightarrow$	
		1077.8	2.2	1.07(20)	$33^- \rightarrow 31^-$	$E2$
	15711.4	1249.7	2.2	0.99(10)	$35^- \rightarrow 33^-$	$E2$
	17139.5	1428.1	1.6		$(37^-) \rightarrow 35^-$	
	18710.3	1570.8	1.1		$(39^-) \rightarrow (37^-)$	
	20414.3	1704.1	0.5		$(41^-) \rightarrow (39^-)$	
	22274.3	1859.5	0.3		$(43^-) \rightarrow (41^-)$	
	24283.3	2010.2	0.1		$(45^-) \rightarrow (43^-)$	
Band 6 (1%)	15129.8	1436.2	1.4	1.12(13)	$33^- \rightarrow 31^-$	$E2$
	16024.0	894.2	0.8	0.74(11)	$34^- \rightarrow 33^-$	$M1/E2$
		888.8	0.7	0.78(15)	$34^- \rightarrow 33^-$	$M1/E2$
	17066.3	1042.3	0.8	1.06(19)	$36^- \rightarrow 34^-$	$E2$
	18305.8	1239.5	1.1	1.18(17)	$38^- \rightarrow 36^-$	$E2$
	19687.6	1381.8	1.1	1.11(21)	$40^- \rightarrow 38^-$	$E2$
	21201.0	1513.4	1.1		$(42^-) \rightarrow 40^-$	
	22866.6	1665.6	0.5		$(44^-) \rightarrow (42^-)$	

TABLE I. (*Continued.*)

Band number (Relative intensity)	$E_i^{\text{level}}$ (keV)	$E_\gamma$ (keV) <sup>a</sup>	Transition intensities <sup>b</sup>	Anisotropy <sup>c</sup> $I_i^\pi \rightarrow I_j^\pi$	Assignment	Multipolarity
	24696.6	1829.3	0.3		(46 <sup>-</sup> ) $\rightarrow$ (44 <sup>-</sup> )	
	26672.0	1975.4	0.1		(48 <sup>-</sup> ) $\rightarrow$ (46 <sup>-</sup> )	
Band 7 (11%)	11556.2	976.7	2.7	1.07(11)	26 <sup>-</sup> $\rightarrow$ 24 <sup>-</sup>	<i>E2</i>
	12231.9	675.7	1.9	1.03(8)	28 <sup>-</sup> $\rightarrow$ 26 <sup>-</sup>	<i>E2</i>
		639.4	2.2	0.90(14)	28 <sup>-</sup> $\rightarrow$ 26 <sup>-</sup>	<i>E2</i>
		874.6	4.1	0.60(5)	28 <sup>-</sup> $\rightarrow$ 27 <sup>-</sup>	<i>M1/E2</i>
		1066.1	0.5		28 <sup>-</sup> $\rightarrow$ 26 <sup>-</sup>	<i>E2</i>
	13041.0	809.1	11.0	1.12(5)	30 <sup>-</sup> $\rightarrow$ 28 <sup>-</sup>	<i>E2</i>
	13949.4	908.4	9.6	1.16(4)	32 <sup>-</sup> $\rightarrow$ 30 <sup>-</sup>	<i>E2</i>
	15030.5	1081.1	7.7	1.23(7)	34 <sup>-</sup> $\rightarrow$ 32 <sup>-</sup>	<i>E2</i>
	16274.1	1243.6	3.3	1.03(12)	36 <sup>-</sup> $\rightarrow$ 34 <sup>-</sup>	<i>E2</i>
	17665.7	1391.6	0.7		(38 <sup>-</sup> ) $\rightarrow$ 36 <sup>-</sup>	
		702.5	0.3		(38 <sup>-</sup> ) $\rightarrow$ (37 <sup>-</sup> )	

<sup>a</sup>The error on the transition energies is 0.2 keV for transitions below 1000 keV and intensities larger than 5% of the <sup>140</sup>Nd channel, 0.5 keV for transitions above 1000 keV and intensities lower than 5%, and 1 keV for transitions above 1200 keV and/or weaker than 1%.

<sup>b</sup>Relative intensities corrected for efficiency, normalized to the sum of the intensities of the 1232.3, 1016.8, 839.5, 962.7, and 144.5 transitions populating the 7<sup>-</sup> isomer and of the 90.5- and 564.2-keV transitions depopulating the first 6<sup>+</sup> state, representing a good estimation of the population of the <sup>140</sup>Nd channel. The transition intensities were obtained from a combination of total projection and gated spectra. The relative errors on the intensities are  $\sim 10\%$  for intensities higher than 1% and up to 50% for intensities below 1%.

<sup>c</sup>The anisotropy has been deduced from two asymmetric  $\gamma\gamma$  coincidence matrices sorted with all detectors on one axis and detectors at 90° and at forward/backward angles, respectively, on the other axis. The tentative spin - parity of the states are given in parenthesis.

ratio by using the  $a_2$  and  $a_4$  angular-distribution coefficients of Ref. [25]. Taking into account the experimental uncertainties, our  $W(\text{f,b})/W(90^\circ)$  ratio can be reproduced with  $\sigma/I$  ranging from 0.3 to 0.7. Larger  $\sigma/I$  values result in smaller quadrupole admixtures that would then also be compatible with *E1* multipolarity for the 190.9-keV transition. Thus, considering the uncertainty in the  $\sigma/I$  ratio, this transition alone would not allow a firm parity assignment to the  $I = 12$  state. However, in view of the presented arguments, we adopt negative parity for this level.

Above the yrast 12<sup>-</sup> state at 4511.6 keV we place a new sequence of three levels with tentative spin-parity assignments of 13<sup>-</sup>, 15<sup>-</sup>, and 17<sup>-</sup>. The (13<sup>-</sup>) state decays by a 868-keV transition that is in coincidence with the strong 867.8-keV (11<sup>-</sup>  $\rightarrow$  9<sup>-</sup>) transition.

The second group of strong transitions populating the 9<sup>-</sup> state at 3452.9 keV was slightly changed based on the coincidence relationships and the newly observed transitions. The 212.9-keV transition was placed above the 720.3- and 922.4-keV [ $R_{\text{DCO}} = 1.04(5)$ ] transitions. This change of placement with respect to Ref. [25] is based on the coincidence relationships, which show that the 212.9-keV transition is not in coincidence with the 173.5-keV transition and is coincident with the cascade of transitions 220.2–1256.0 keV, which exclude the placement just above the 9<sup>-</sup> state as given in Ref. [25]. In this way the four new transitions populating and deexciting the two  $I = 11$  states at 4912.1 and 4875.4 keV may be placed as follows: 183.5 keV [ $R_{\text{DCO}} = 0.53(2)$ ] (12<sup>-</sup>  $\rightarrow$  11<sup>+</sup>), 220.2 keV [ $R_{\text{DCO}} = 0.56(3)$ ] (12<sup>-</sup>  $\rightarrow$  11<sup>-</sup>), 1292.8 keV [ $R_{\text{DCO}} = 0.33(3)$ ] (11<sup>+</sup>  $\rightarrow$  10<sup>+</sup>), 702.2 keV (11<sup>-</sup>  $\rightarrow$  10<sup>-</sup>) [ $R_{\text{DCO}} = 0.33(4)$ ], and 1256.0 keV (11<sup>-</sup>  $\rightarrow$  10<sup>+</sup>). The 240.6-keV [ $R_{\text{DCO}} = 0.59(1)$ ] transition reported

in Ref. [25] was moved up by 1541.1 keV and populates the (18) state at 7944.7 keV. We confirm the parallel 961.8-keV [ $R_{\text{DCO}} = 1.04(12)$ ]–173.5-keV [ $R_{\text{DCO}} = 0.56(2)$ ] cascade connecting the 13<sup>-</sup> and 10<sub>2</sub><sup>-</sup> states and the 544.3-keV [ $R_{\text{DCO}} = 0.46(2)$ ] (16<sup>-</sup>  $\rightarrow$  15<sup>-</sup>) transition. Above the 13<sup>-</sup> state we also confirm the sequence of the 119.7-keV (14<sup>-</sup>  $\rightarrow$  13<sup>-</sup>) and 181.6-keV (15<sup>-</sup>  $\rightarrow$  14<sup>-</sup>) transitions, which from the angular-distribution measurements of Ref. [25] results to be mixed *M1/E2* transitions. In the low-spin part of the level scheme we identify a cascade of quadrupole transitions built on the 6<sup>+</sup> state, consisting of the 818.2-keV [ $R_{\text{DCO}} = 0.89(15)$ ] and 971.4-keV [ $R_{\text{DCO}} = 0.87(16)$ ] transitions, leading to a 10<sup>+</sup> state at 4154.7 keV. The 8<sup>+</sup> state of this cascade decays also to the 7<sup>-</sup> isomeric state through the 962.7-keV *E1* transition.

On top of the 4154.7-keV 10<sup>+</sup> state we place the 1108.5-keV transition that depopulates another sequence of transitions, with energies of 154.4 [ $R_{\text{DCO}} = 0.53(3)$ ], 204.8 [ $R_{\text{DCO}} = 0.53(5)$ ], and 531.9 [ $R_{\text{DCO}} = 0.51(7)$ ] keV, leading to a 6154.3-keV state. The observed sequence built on the 6<sup>+</sup> state up to the 6154.3-keV level is seen in coincidence with higher-lying states, but the connecting transitions could not be identified.

The level scheme above the previously observed highest-spin states [25] contains several high-energy  $\gamma$ -ray transitions. These are the relatively strong transitions with energies of 1653.7 [ $R_{\text{DCO}} = 1.25(11)$ ], 1366.2 [ $R_{\text{DCO}} = 1.15(12)$ ], 1442.2 [ $R_{\text{DCO}} = 1.04(12)$ ], and 1352.2 [ $R_{\text{DCO}} = 1.16(11)$ ] keV, and also the weaker ones of 1337.7, 1216.3, and 1246.5 keV, as well as those feeding the 6403.7-keV state mentioned above. The composite cluster and clover detectors of the EUROBALL array [26] have high efficiency, after add-back,

TABLE II. Spectroscopic information for the floating bands in  $^{140}\text{Nd}$ .

Band number (Relative intensity)	$E_\gamma$ (keV) <sup>a</sup>	Transition intensities <sup>b</sup>
Band 8 (1%)	954.5	0.8
	1113.1	1.0
	1312.9	0.5
	1522.9	0.4
	1705.0	0.3
Band 9 (0.8%)	1023.0	0.3
	1142.6	0.8
	1295.3	0.7
	1470.6	0.5
	1669.7	0.4
Band 10 (0.5%)	1846.8	0.3
	838.0	0.5
	971.7	0.5
	1095.6	0.5
	1281.6	0.5
Band 11 (2%)	1477.6	0.5
	1623.0	0.3
	1026.0	1.4
	798.6	2.2
	1016.3	1.9
	1243.2	1.6
Band 12 (5.5%)	1485.2	1.4
	1717.6	1.1
	1925.6	0.5
	2134.1	0.3
	1059.1	5.5
	1318.4	4.1
	1542.1	1.9
	1734.7	0.8
	1921.4	0.3

<sup>a</sup>The error on the transition energies is 0.2 keV for transitions below 1000 keV and intensities larger than 5% of the  $^{140}\text{Nd}$  channel, 0.5 keV for transitions above 1000 keV and intensities lower than 5%, and 1 keV for transitions above 1200 keV and/or weaker than 1%.

<sup>b</sup>Relative intensities corrected for efficiency, normalized to the sum of the intensities of the 1232.3, 1016.8, 839.5, 962.7, and 144.5 transitions populating the  $7^-$  isomer and of the 90.5- and 564.2-keV transitions depopulating the first  $6^+$  state, representing a good estimation of the population of the  $^{140}\text{Nd}$  channel. The transition intensities were obtained from a combination of total projection and gated spectra. The relative errors on the intensities are  $\sim 10\%$  for intensities higher than 1% and up to 50% for intensities below 1%.

for the detection of high-energy  $\gamma$  rays, which facilitated the construction of the level scheme in the energy range around 7 MeV. In this range of excitation energy the decay pattern is very complex, and the difficulty of consistently fitting the transition intensities suggests the presence of several isomeric states with lifetimes larger than several tens of nanoseconds. However, we have been able to extract  $R_{\text{DCO}}$  values for the transitions that are essential for the spin-parity assignment of the higher-lying bands and are given in what follows. The transitions leading to the  $22^{(+)}$  assignment for the lowest state

in band 3, lying between the  $18^-$  state at 7520.3 keV and the  $22^{(+)}$  state at 9562.8 keV, have the following  $R_{\text{DCO}}$  values: 797.1 ( $19^- \rightarrow 18^-$ ) [ $R_{\text{DCO}} = 0.60(2)$ ], 282.1 ( $20^{(+)} \rightarrow 19^-$ ) [ $R_{\text{DCO}} = 0.51(1)$ ], 429.6 ( $21^{(+)} \rightarrow 20^{(+)}$ ) [ $R_{\text{DCO}} = 0.38(3)$ ], and 534.0 ( $22^{(+)} \rightarrow 21^{(+)}$ ) [ $R_{\text{DCO}} = 0.44(2)$ ].

The spin-parity assignment of the band of dipole transitions built on the  $22^{(+)}$  state at 9665.4 keV have the following  $R_{\text{DCO}}$  values: 531.4 ( $22^{(+)} \rightarrow 21^{(+)}$ ) [ $R_{\text{DCO}} = 0.47(5)$ ], 325.7 ( $23^{(+)} \rightarrow 22^{(+)}$ ) [ $R_{\text{DCO}} = 0.48(3)$ ], 221.0 ( $23^{(+)} \rightarrow 22^{(+)}$ ) [ $R_{\text{DCO}} = 0.60(4)$ ], 371.0 ( $24^{(+)} \rightarrow 23^{(+)}$ ) [ $R_{\text{DCO}} = 0.36(6)$ ], 477.4 ( $25^{(+)} \rightarrow 24^{(+)}$ ) [ $R_{\text{DCO}} = 0.46(1)$ ], and 571.2 ( $26^{(+)} \rightarrow 25^{(+)}$ ) [ $R_{\text{DCO}} = 0.47(9)$ ].

The spin-parity of bands 1, 2, 5, 6, and 7 are determined by the transitions connecting band 1 to low-lying states with known spin-parity (see Fig. 1), which have the following  $R_{\text{DCO}}$  values: 612.8 ( $20^- \rightarrow 18^-$ ) [ $R_{\text{DCO}} = 1.08(22)$ ], 845.8 ( $18^- \rightarrow 17^-$ ) [ $R_{\text{DCO}} = 0.52(3)$ ], and 756.0 ( $18^- \rightarrow 17^-$ ) [ $R_{\text{DCO}} = 0.41(6)$ ].

Above spin  $I \approx 20$ , we observe several well-defined cascades without strong inter-connecting transitions; see the high-spin part of the level scheme displayed in Fig. 2. The stronger bands, 1–7, are linked to lower-lying states in the level scheme, but the weaker bands, 8–12, could not be connected to lower levels. The strongest structure, band 1, starts with the  $21^-$  state at 9166.6 keV and after a crossing at spin  $33^-$  continues with band 6 up to the highest observed state of normal deformation with spin-parity  $48^-$  and an energy of 26.67 MeV. It decays into band 2 by means of the 734.2-keV [ $R_{\text{DCO}} = 0.57(4)$ ], 527.3-keV [ $R_{\text{DCO}} = 0.64(3)$ ], and 449.5-keV transitions. Band 5 with the highest state of spin  $45^-$  at an excitation energy of 24.28 MeV decays into band 1. Band 7 decays toward bands 1 and 2 through a series of three intermediate states that could be a part of another band only partially observed in the experiment. The  $32^-$  and  $34^-$  states at 13.95 and 15.03 MeV, respectively, are populated by transitions from several non-yrast levels. Band 4 decays into band 3 by means of the 325.6- [ $R_{\text{DCO}} = 0.48(3)$ ], 400.9-, and 772.9-keV transitions, and band 3 is connected to lower-lying states, feeding into the bottom of band 2 and by means of an irregular sequence of transitions into the  $18^-$  state at 7520.3 keV.

The excitation energies and spins of floating bands 8–12 could not be determined. However, they are firmly assigned to  $^{140}\text{Nd}$ , since the transitions observed in coincidence with the bands are low-lying transitions in  $^{140}\text{Nd}$ . Bands 8–11 decay mainly toward the  $27^-$  state of band 1, while band 12 decays mainly toward the  $20^-$  state of band 2. A high-spin SD band, extending up to  $I = 66$ , was established but could not be connected to lower-lying states. Results on this band have been published recently [20].

#### IV. DISCUSSION

The level scheme of  $^{140}\text{Nd}$  shows three distinctly different features. The energies of the strongly populated excited states are plotted as functions of spin in Fig. 4. At low and medium spin an irregular pattern, typical for spherical or near-spherical nuclei, is observed. The medium- to high-spin region is

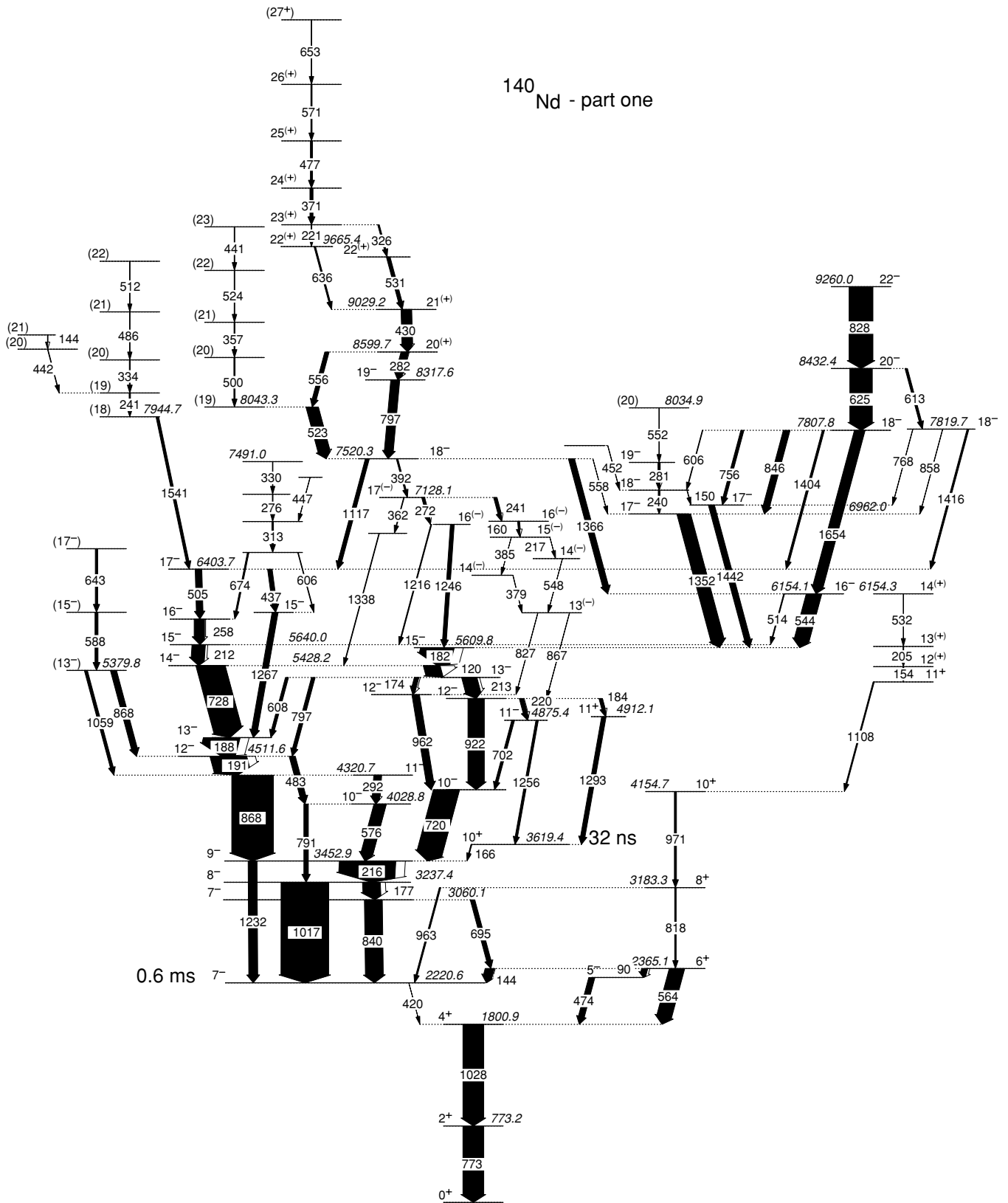


FIG. 1. Low- and medium-spin parts of level scheme of  $^{140}\text{Nd}$  based on the results from the present experiment and on previous work [25].

dominated by regular band structures as normally found in deformed nuclei. The highest spins in this nucleus are observed in a SD band. In the following subsections we therefore divide

the discussion into two parts, the first one for the spherical level scheme and the second one for the deformed – as we shall argue – triaxial band structures.

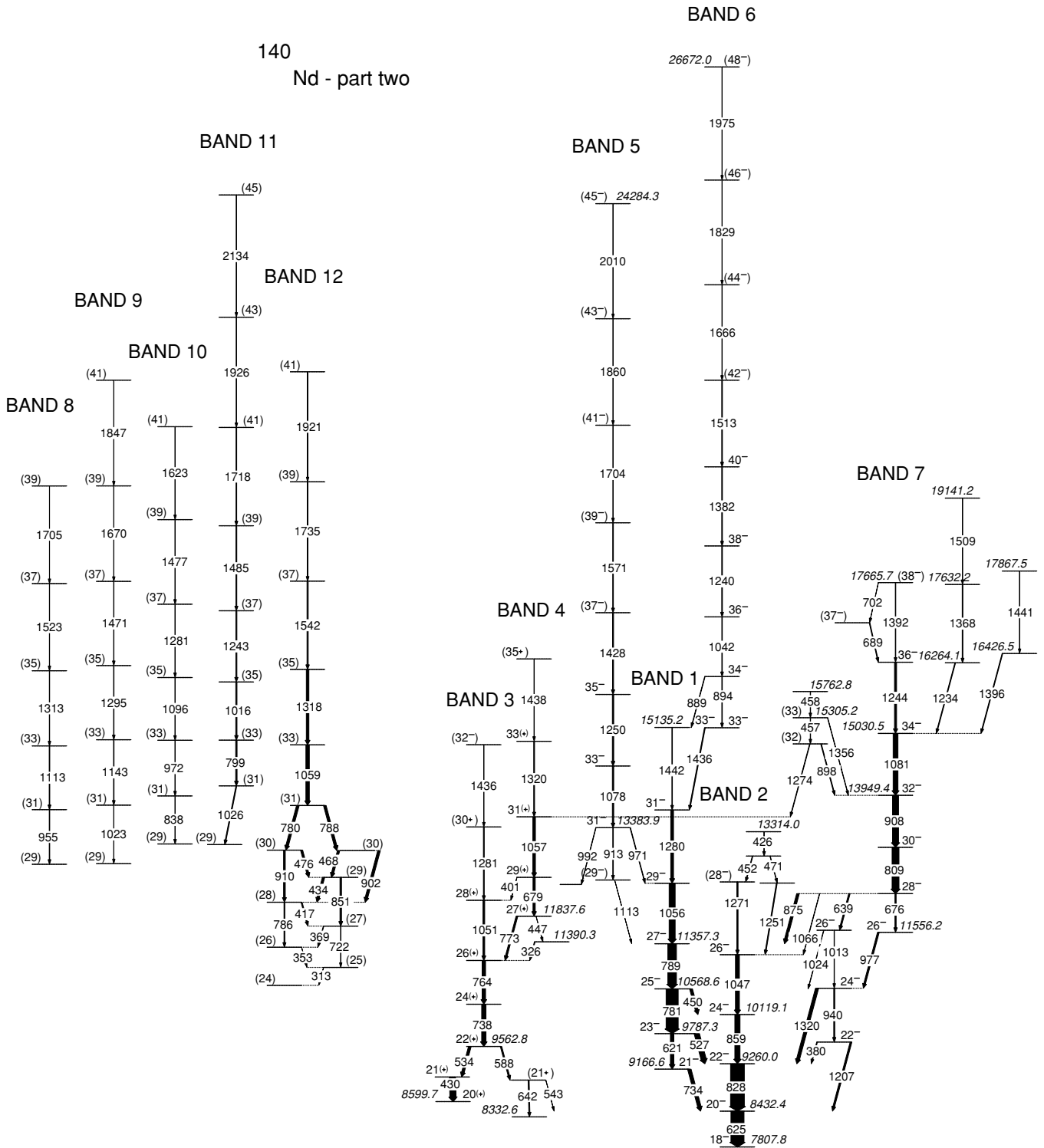


FIG. 2. Medium- and high-spin parts of level scheme of <sup>140</sup>Nd, based on the results of the present experiment.

**A. Spherical low- and medium-spin levels**

The level structure of <sup>140</sup>Nd at relatively low spin was previously interpreted by use of shell-model calculations, including two-particle-hole excitations with a residual surface  $\delta$ -interaction [25]. The first 2<sup>+</sup> and 4<sup>+</sup> states were assumed to be collective vibrations, while the higher-lying states up

to the first 10<sup>+</sup> state were interpreted as two-proton-particle or two-neutron-hole excitations in the orbitals around the Fermi level. The proton orbitals that can be occupied at low spins for spherical and triaxial deformations are  $\pi d_{5/2}$ ,  $\pi g_{7/2}$ , and  $\pi h_{11/2}$  above the Z = 50 shell closure, while the occupied neutron orbitals are below the N = 82 shell closure:  $\nu d_{3/2}^{-1}$ ,  $\nu s_{1/2}^{-1}$ ,  $\nu h_{11/2}^{-1}$ ,  $\nu d_{5/2}^{-1}$ ,  $\nu g_{7/2}^{-1}$ . The first two-neutron states

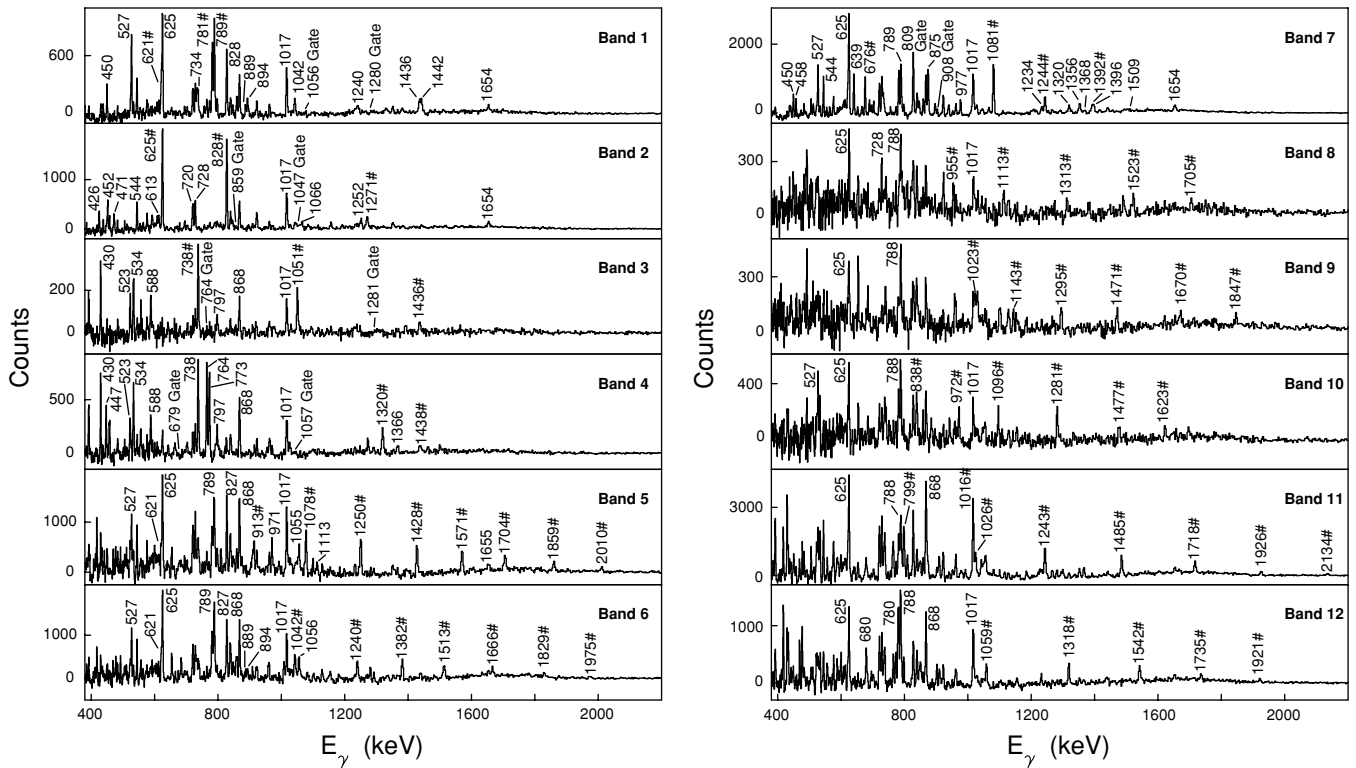


FIG. 3. Gamma-ray coincidence spectra of the new bands in  $^{140}\text{Nd}$ . The spectra were obtained by double gating on combinations of transitions indicated in the different panels. For the spectra with no gate indications, double gates on all transitions were set except for the highest one in the band. The in-band transitions are marked with a # symbol.

that are also observed in the neighboring  $N = 80$  nuclei are the  $7^-$  and  $10^+$  isomers having  $(\nu h_{11/2}^{-1} \nu d_{3/2}^{-1})_{7^-}$  and  $(\nu h_{11/2}^{-2})_{10^+}$  configurations, respectively, and the  $5^-$  state having a mixed  $[\nu h_{11/2}^{-1} (\nu s_{1/2}^{-1} / \nu d_{3/2}^{-1})]_{5^-}$  configuration. The next

higher-energy two-neutron states with spins  $7^-$ ,  $8^-$ , and  $9^-$  have the mixed  $[\nu h_{11/2}^{-1} (\nu d_{5/2}^{-1} / \nu g_{7/2}^{-1})]_{7^-, 8^-, 9^-}$  configurations. The first two-proton excitations are present in the  $4^+$  state of mainly vibrational character and in the  $6^+$  state through the  $(\pi d_{5/2} \pi g_{7/2})_{6^+}$  configuration.

The level structure up to spins around 20 is irregular, and often the decay of a given level is highly fragmented. It is dominated by quadrupole vibrations (the excitation energy of the first  $2^+$  state is 773 keV) built on the simple two-particle excitations or by four-particle excitations involving the two-proton and two-neutron states present at low spins. From the decay pattern and the level spacing with respect to low-lying levels, configurations for the following states can be suggested:

- (i)  $10^-$  at 4029 keV:  $8^- \otimes 2^+$  ( $E_{8^-} + E_{2^+} = 4013$  keV),
- (ii)  $11^-$  at 4321 keV:  $9^- \otimes 2^+$  ( $E_{9^-} + E_{2^+} = 4228$  keV),
- (iii)  $12^-$  at 4512 keV:  $7^- \otimes 6^+$  ( $E_{7^-} + E_{6^+} = 4586$  keV),
- (iv)  $13^-$  at 4700 keV:  $7^- \otimes 6^+$  ( $E_{7^-} + E_{6^+} = 4586$  keV),
- (v)  $12^-$  at 5096 keV:  $7_2^- \otimes 6^+$  ( $E_{7_2^-} + E_{6^+} = 5425$  keV),
- (vi)  $13^-$  at 5309 keV:  $7_2^- \otimes 6^+$  ( $E_{7_2^-} + E_{6^+} = 5425$  keV),
- (vii)  $14^-$  at 5428 keV:  $8^- \otimes 6^+$  ( $E_{8^-} + E_{6^+} = 5603$  keV),
- (viii)  $15^-$  at 5610 keV:  $9^- \otimes 6^+$  ( $E_{9^-} + E_{6^+} = 5818$  keV).

### B. Collective high-spin states

The high-spin level scheme of  $^{140}\text{Nd}$  is dominated by rather regular band structures with an energy separation between consecutive transitions of either  $\approx 150$  keV or  $\geq 200$  keV. The

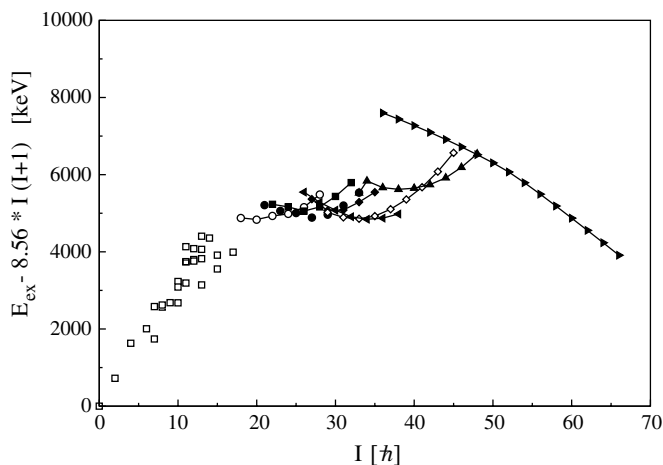


FIG. 4. Excitation energies relative to a rigid-rotor reference as a function of spin for strongly populated states in  $^{140}\text{Nd}$ . Some of the spherical states are shown as open squares. The collective bands are connected by curves. The energy of the SD band observed at the highest spins and of the floating triaxial bands are not determined experimentally, but estimated on the basis of the entry point into the low-lying states.

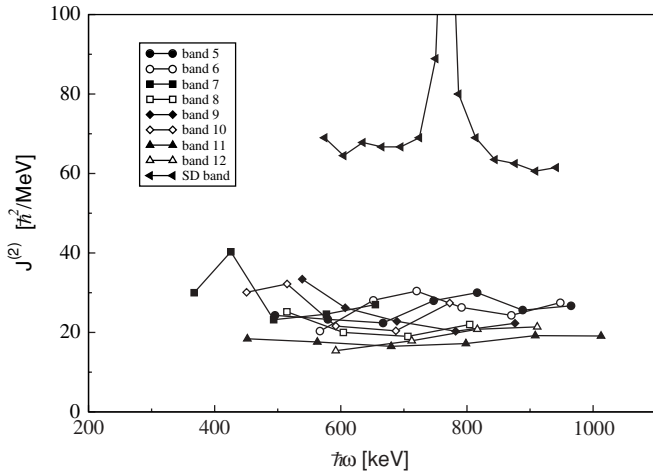


FIG. 5. Dynamic moments of inertia of the high-spin bands in  $^{140}\text{Nd}$ .

dynamic moments of inertia of the long new bands 5–12 are shown in Fig. 5. These moments of inertia are much smaller than that of the SD band in  $^{140}\text{Nd}$  [20]. The SD band shows a crossing around a rotational frequency of 770 keV. Bands with dynamic moments of inertia around  $20 \hbar^2\text{MeV}^{-1}$  were also observed in the lighter Nd isotopes [16]. The bands in  $^{138}\text{Nd}$  and  $^{139}\text{Nd}$  were interpreted as triaxial structures, and we propose a similar interpretation for  $^{140}\text{Nd}$ . In Fig. 6,

PESs calculated for  $^{140}\text{Nd}$  in the CNS formalism, [6,9,31] are shown. The surfaces are drawn for  $I^\pi = 31^-, 41^-, 51^-$ , and  $61^-$ , i.e., for negative parity and signature  $\alpha = 1$ , but they do not look much different for other combinations of parity and signature. At  $I = 31$ , the lowest-energy minimum corresponds to a shape that is close to spherical but with secondary minima at triaxial shape ( $\epsilon = 0.20\text{--}0.25, \gamma \approx 30^\circ$ ) and at SD shape ( $\epsilon \approx 0.45, \gamma \approx 0^\circ$ ). These three minima survive at  $I = 41$ , but now the triaxial minimum corresponds to lowest energy. It is then not possible to generate much higher spins close to spherical shape, and therefore only the triaxial and the SD minima are seen for higher spins, with the two minima about equally deep for  $I = 51$ . For  $I = 61$  the SD minimum is clearly the lowest. Note that the different minima essentially stay at the same deformation independent of the spin value; their relative energies, instead, are strongly dependent on spin. If a specific configuration is chosen, only one minimum will be seen (see, e.g., Fig. 6 of Ref. [16]) and, by following the energy of this minimum, we get the  $E - E_{\text{rot}}$  vs.  $I$  curves for specific configurations discussed below.

We argue in the following discussion that the high-spin bands of  $^{140}\text{Nd}$  shown in Fig. 3 are associated with the triaxial minima, while the SD band discussed in Ref. [20] was assigned to the strongly deformed minimum at  $\epsilon \approx 0.45, \gamma \approx 0^\circ$ .

Within the CNS formalism, pairing is neglected. Thus it is mainly applicable to high-spin states. Configurations are fixed by the number of particles with signature  $\alpha = 1/2$  and

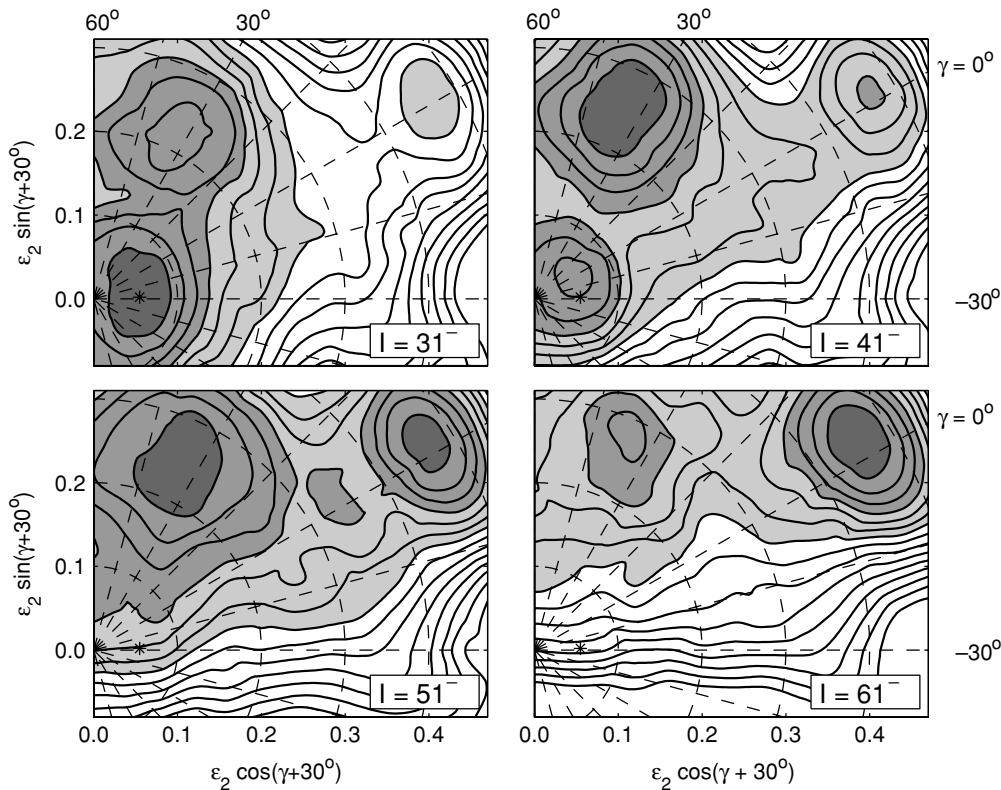


FIG. 6. PESs calculated for  $^{140}\text{Nd}$  at spin  $I = 31\text{--}61$  with negative parity and signature  $\alpha = 1$ . The contour-line separation is 0.5 MeV. Note the coexistence of three minima that are essentially unchanged in deformation (except that the close-to-spherical minimum disappears at the highest-spin values), but with relative energies that are strongly dependent on spin.

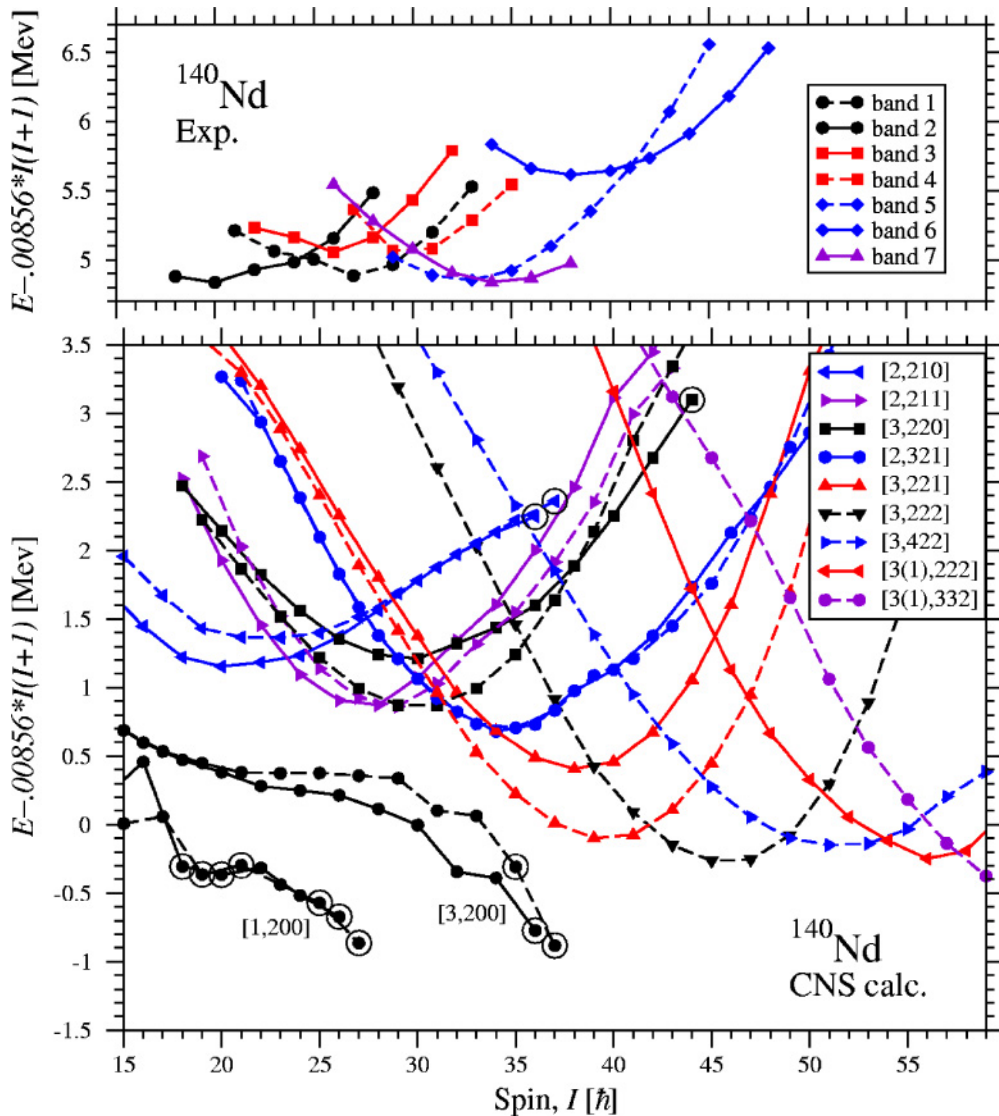


FIG. 7. (Color online) The observed bands 1–7 in  $^{140}\text{Nd}$  for which spins and excitation energies are determined (upper panel) and lowest-lying calculated negative-parity bands labeled according to Eq. (1) (lower panel) plotted relative to a standard rotating reference core. The bands are drawn with solid curves for signature  $\alpha = 0$  and dashed curves for  $\alpha = 1$ . For the calculated bands, signature partners are generally shown at low spins while only the lowest signature is included at high spin. At high spins, beyond  $I \approx 50$ , SD bands become yrast, as indicated in Fig. 4. They are not included in the present figure but were drawn in Fig. 5 of Ref. [20].

$\alpha = -1/2$  in the different shells ( $N_{\text{rot}}$  shells) of the rotating harmonic-oscillator Hamiltonian. Furthermore, a distinction is made between orbitals dominated by high- $j$  intruder subshells and other subshells, respectively.

The CNS formalism has been applied to the terminating bands in the  $A = 110$  and  $A = 150$  regions; see, e.g. [6,7,32] and references therein. These applications have resulted in a detailed understanding of the terminating bands and of the role of different orbitals, e.g., how they contribute in building the angular momentum and the shape of the nucleus. The  $^{140}\text{Nd}$  nucleus falls in between these two regions, which means that the orbitals with an active role in building its high-spin states at small and intermediate deformation are also active either in the  $A = 110$  or the  $A = 150$  region. Thus we can use the understanding obtained from the terminating bands to get a general idea about what kind of bands to expect in

$^{140}\text{Nd}$ . In particular, it turns out that many orbitals drive toward positive- $\gamma$  values, but there are a few orbitals that counteract the final transition toward noncollective states at  $\gamma = 60^\circ$ . Thus, even though it turns out to be difficult to give any definite predictions about the configurations of the observed bands, the general agreement gives very strong evidence that these bands are indeed triaxial.

The configurations in  $^{140}\text{Nd}$  are conveniently labeled by the number of high- $j$  particles and holes relative to a  $Z = 50$  and  $N = 82$  core;

$$[p_1, n_1 n_2 n_3] \equiv \pi(h_{11/2})^{p_1} v(h_{11/2})^{-n_1} v(h_{9/2} f_{7/2})^{n_2} (i_{13/2})^{n_3}. \quad (1)$$

The number of protons in the  $g_{7/2}$  and  $d_{5/2}$  subshells and neutron holes in the  $d_{3/2}$  and  $s_{1/2}$  subshells, respectively, is then determined from the fixed number of particles,  $Z = 60$  and

$N = 80$  for  $^{140}\text{Nd}$ . A few of the lowest-lying positive-parity triaxial bands calculated within this formalism were published in our previous work [20].

The energies of the experimentally observed bands with known spins and energies, bands 1–7, and of the calculated bands are plotted with respect to a standard reference core in Fig. 7. Bands 5–7 are rather regular and extend to the highest spins (see upper panel). Therefore we interpret them within the unpaired CNS formalism. The observed bands have negative parity and should be compared with the low-lying calculated negative-parity bands (see lower panel of Fig. 7). As outlined above, the neutron configurations of these bands are characterized by holes in the  $N = 82$  core and particles in the high- $j$  orbitals above the  $N = 82$  gap. There is a high density of calculated bands in the yrast region with the lowest ones shown in the figure. All these bands are built in the triaxial minimum of Fig. 6, corresponding to a deformation with  $\gamma \approx 30^\circ$ . The triaxiality is understood from the shape-driving effects of the different particles. The particles in high- $j$  orbitals are relatively easy to align and tend to induce an oblate shape distribution with  $\gamma = 60^\circ$ . However, this tendency will be counterbalanced by the neutron holes below the  $N = 82$  gap, which tend to polarize the nucleus toward  $\gamma < 0^\circ$ . The additional particles in open shells, i.e., the  $g_{7/2}/d_{5/2}$  protons, will not have any strong  $\gamma$ -driving effects, but will contribute to the collectivity. Combining these different effects leads to well-defined and relatively deep minima at  $\gamma \approx 30^\circ$ .

With an increasing number of particle-hole excitations across the  $N = 82$  gap, the favored energies of the bands move to higher and higher spins, as seen in Fig. 7. In this process, the optimal proton configuration gradually increases its number of high- $j$  particles from two  $h_{11/2}$  particles, to three  $h_{11/2}$  particles, and finally to configurations including one  $i_{13/2}$  proton for spin above  $I = 50$ . For spin values around the minima, the bands have a stable triaxial deformation with  $\gamma = 30^\circ$ – $40^\circ$  (see our Fig. 6 and Fig. 6 of Ref. [16]) but some bands can be followed to a terminating aligned state (encircled) at a relatively high excitation energy. The calculated bands at relatively low spin with no neutrons excited across the  $N = 82$  gap ([1,200] and [3,200]) have different properties and are built in the close-to-spherical minimum of Fig. 6.

The experimental bands 5 and 7 have their energy minima at  $I \approx 33$  and  $I \approx 34$ , respectively; see Fig. 7. Therefore, comparing with theory, the most probable configurations of these bands appear to be either [3,220] or [2,321]. Band 6 with its minimum at  $I \approx 38$  would rather be interpreted as [3,221]. Note, however, that with this interpretation, we do not reproduce the relative energies between the bands. Nevertheless, according to the general features of the calculations, only triaxial structures can account for the observed high-spin bands.

It is interesting to consider in more detail how the spin is built in these triaxial bands. It turns out that, at the large triaxiality, the high- $j$  particles are close to fully aligned already at low frequencies while the  $d_{5/2}/g_{7/2}$  protons and the  $h_{11/2}$  neutron holes align more or less linearly with rotational frequency and the spin contribution from the  $d_{3/2}/s_{1/2}$  neutron holes is essentially negligible. Thus, at low-spin values, these bands are relatively high above yrast because of the energy cost to excite particles to the high- $j$  orbitals. However, higher spins

can be obtained at a low energy cost when these particles align their angular momenta, so that at the spin value where these particles are more or less fully aligned, these bands become favored in energy relative to other configurations at the same spins. Then, at even higher spin values, it becomes relatively expensive in energy to align the remaining spin vectors so that the band goes away from yrast.

The analysis above suggests that the spin that can be built from the high- $j$  particles should be correlated with the spin values at which the bands are most favored in energy, which corresponds to the minima in Fig. 7. Therefore we plot the maximum spin contribution from the high- $j$  particles versus the spin value at this minimum in Fig. 8 for the calculated bands. As anticipated above, there is a linear relation between these two quantities in the whole spin range, with typical deviations of  $\pm 2$ . Assuming that the suggested configurations are a correct description of the experimental bands, we can deduce an approximate spin contribution from high- $j$  particles in the observed bands 5, 6, and possibly 7. With the minima at  $I \approx 33, 34$ , and  $38$ , we conclude that the maximum spin contribution from the aligned particles amounts to 23–26 for the three bands. For the configurations suggested above, the expected contribution is  $10 + 8 + 6.5 = 24.5$  for the  $h_{11/2}$  protons,  $h_{9/2}/f_{7/2}$  neutrons, and  $i_{13/2}$  neutrons in the [2,321] configuration,  $13.5 + 8 = 21.5$  in the [3,220] configuration, and  $13.5 + 8 + 6.5 = 28$  for those  $j$  shells in the [3,221] configuration. These values appear consistent with those deduced from the line fit in Fig. 8 within the uncertainty of  $\pm 2$ .

It is also instructive to analyze the bands in a plot of spin  $I$  as functions of transition energy  $E_\gamma$ , shown in Fig. 9 (note that the rotational frequency equals  $E_\gamma/2$ ). The three linked high-spin bands 5, 6, and 7 are then seen as essentially straight lines

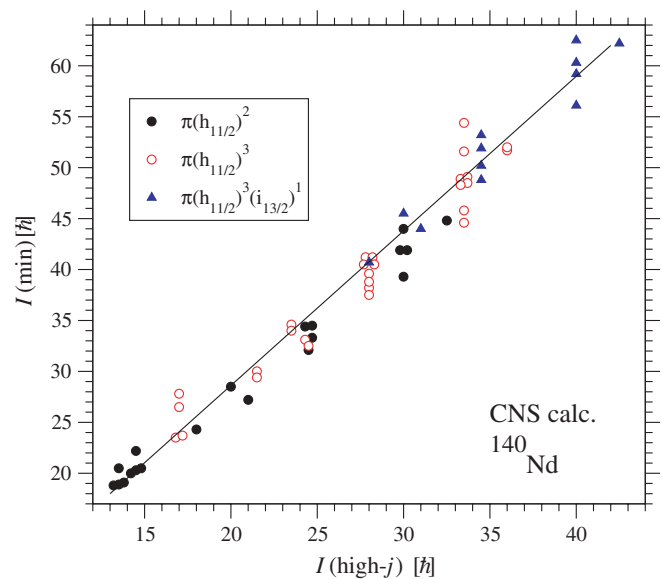


FIG. 8. (Color online) The spin of the minima taken from the theory (see Fig. 7) as a function of the spin contribution from high- $j$  particles in the respective configurations. Proton configurations  $(h_{11/2})^2$ ,  $(h_{11/2})^3$ , and  $(h_{11/2})^3(i_{13/2})^1$  are indicated by filled circles, open circles, and filled triangles, respectively. Neutron configurations starting from those of the type  $(h_{9/2}f_{7/2})^1$  up to  $(h_{9/2}f_{7/2})^3(i_{13/2})^2$  are included.

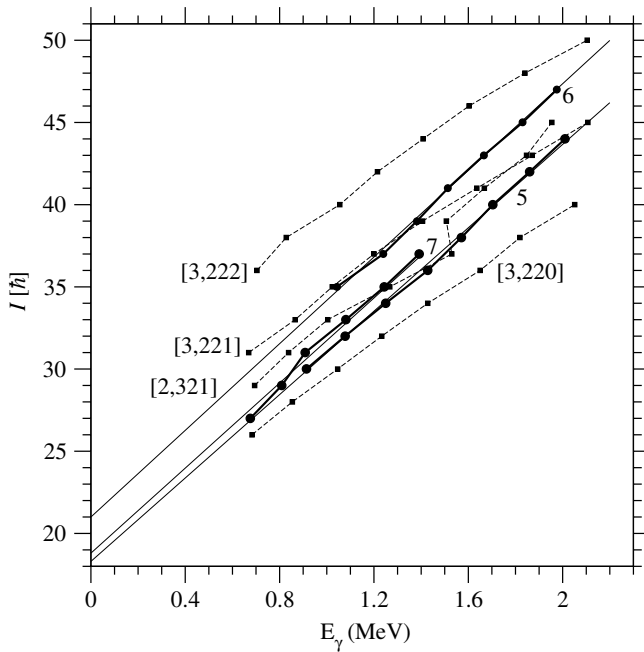


FIG. 9. Spin vs. transition energy for bands 5, 6, and 7 compared with the curves for a few low-lying calculated bands. The observed bands are drawn with big symbols and heavy curves while the calculated bands are drawn with smaller squares and thin dashed curves. The thin solid lines are used to follow the slopes of bands 5, 6, and 7 to zero frequency. The discontinuity in the [2,321] configuration is caused by a “crossing” between the fourth and the fifth low- $j$ ,  $N = 4$ ,  $\alpha = 1/2$  orbitals.

that cut the  $E_\gamma = 0$  axis at a large spin value that corresponds to the “alignment at no rotation.” These values come out as  $\sim 18$ ,  $19$ , and  $21$  for bands 5, 7, and 6, respectively, and might be compared with the maximum spin contribution from the high- $j$  particles in the corresponding configurations:  $21.5$  and  $24.5$  for the [3,220] and [2,321] configurations assigned to bands 5 and 7, respectively, and  $28$  for [3,221] assigned to band 6. This comparison is consistent with our general expectation that the high- $j$  particles are almost fully aligned at very small rotational frequencies.

The  $I$  vs.  $E_\gamma$  curves for a few of the low-lying calculated configurations are also shown in Fig. 9. There is a reasonable agreement between experiment and calculations, even if there is a somewhat larger discrepancy for band 7 for which the configuration [3,221] with a high- $j$  spin contribution of  $28$  was suggested above. The slopes of the calculated curves in Fig. 9 are somewhat smaller than those of the observed bands and mainly depend on the orbitals of the low- $j$  particles and

holes. For example, if a neutron hole is put in an  $h_{11/2}$  orbital instead of in an  $N = 4$  orbital, the slope increases because it becomes easier to build angular momentum. This is understood from the fact that the  $N = 4$  holes are placed in orbitals of  $s_{1/2}$  and  $d_{3/2}$  characters that contribute very little angular momentum, contrary to the  $h_{11/2}$  holes. Note also that the slopes in Fig. 9, which are drawn for the observed bands in Fig. 5, are directly proportional to the  $\mathcal{J}^{(2)}$  moment of inertia.

With a general understanding of bands 5, 6, and 7, it appears reasonable to assume that the less-regular and lower-spin bands, 1–4, are built from similar configurations but with fewer high- $j$  particles. With their minima in Fig. 7 in the spin range of  $I = 20$ – $30$  and with negative parity, they would then be assigned to configurations of the types [2,210], [2,211], and [3,220], which are built in the close-to-spherical minimum of Fig. 6. These configurations are generally of the same type as those assigned to the observed  $I = 10$ – $20$  states and are clearly calculated to be yrast for spin values up to  $I \approx 35$ , but no corresponding experimental bands have been observed. This clearly suggests that these configurations are calculated too low in energy. However, there is still the possibility that they are present close to the yrast line and one reason why they have not been observed is their smaller collectivity.

## V. SUMMARY

In summary, we established the level scheme of  $^{140}\text{Nd}$  up to  $I = 48$ , identifying a large number of rotational bands with relatively low moments of inertia. The general features of the level scheme up to spin  $\sim 15$  were discussed in terms of shell-model excitations, whereas the regular rotational cascades at higher spins were interpreted by configuration-dependent CNS calculations as being built on triaxial shapes with normal deformation,  $\epsilon_2 \approx 0.25$ , and maximal triaxiality,  $\gamma \approx +30^\circ$ .

## ACKNOWLEDGMENTS

The authors are grateful to the technical staff at the Institut de Recherches Subatomiques involved in running the Vivitron accelerator and the EUROBALL array. The work was supported by Bundesministerium für Bildung, Forschung und Technologie, Germany, under contract no. 06 BN 907, by the EU (European Union) under contract no. HPRI-CT-1999-00078, by the Italian National Institute of Nuclear Physics, by the Danish Science Foundation, by the Swedish Science Research Council, and by the U.S. Department of Energy under contract no. DE-AC03-76SF00098.

- [1] A. Bohr and B. R. Mottelson, *Nuclear Structure* (Benjamin, New York, 1975), Vol 2.
- [2] S. Frauendorf, *Rev. Mod. Phys.* **73**, 463 (2001).
- [3] G. B. Hagemann, *Eur. Phys. J. A* **20**, 183 (2004).
- [4] C. M. Petrache, *Eur. Phys. J. A* **20**, 39 (2004).
- [5] K. Starosta, T. Koike, C. J. Chiara, D. B. Fossan, D. R. LaFosse, A. A. Hecht, C. W. Beausang, M. A. Caprio, J. R. Cooper, R. Krücken, J. R. Novak, N. V. Zamfir, K. E. Zyranski,

- D. J. Hartley, D. Balabanski, J. Y. Zhang, S. Frauendorf, and V. I. Dimitrov, *Phys. Rev. Lett.* **86**, 971 (2001).
- [6] A. V. Afanasjev, D. B. Fossan, G. J. Lane, and I. Ragnarsson, *Phys. Rep.* **322**, 1 (1999).
- [7] W. Satula and R. A. Wyss, *Rep. Prog. Phys.* **68**, 131 (2005).
- [8] I. Ragnarsson, A. Sobczewski, R. K. Sheline, S. E. Larsson, and B. Nerlo-Pomorska, *Nucl. Phys.* **A233**, 329 (1974).

- [9] A. V. Afanasjev and I. Ragnarsson, Nucl. Phys. **A608**, 176 (1996).
- [10] R. Bengtsson: <http://www.matfys.lth.se/~ragnar/ultimate.html>
- [11] T. Bengtsson, Nucl. Phys. **A496**, 56 (1989); **A512**, 124 (1990).
- [12] B. Singh, R. Zywna, and R. B. Firestone, Nucl. Data Sheets **97**, 241 (2002).
- [13] R. B. Firestone, *Table of Isotopes*, edited by V. S. Shirley *et al.* (Wiley, New York, 1999).
- [14] D. T. Joss, E. S. Paul, R. M. Clark, I. Y. Lee, S. J. Asztalos, J. A. Becker, L. Bernstein, B. Cederwall, M. A. Deleplanque, R. M. Diamond, R. Fallon, L. P. Farris, K. Hauschild, I. M. Hibbert, W. H. Kelly, A. O. Macchiavelli, P. J. Nolan, N. J. O'Brien, A. T. Semple, F. S. Stephens, and R. Wadsworth, Phys. Rev. C **58**, 3219 (1998).
- [15] N. J. O'Brien, A. Galindo-Uribarri, V. P. Janzen, D. T. Joss, P. J. Nolan, C. M. Parry, E. S. Paul, D. C. Radford, R. Wadsworth, and D. Ward, Phys. Rev. C **59**, 1334 (1999).
- [16] C. M. Petrache, G. Lo Bianco, D. Ward, A. Galindo-Uribarri, P. Spolaore, D. Bazzacco, T. Kröll, S. Lunardi, R. Menegazzo, C. Rossi Alvarez, A. O. Macchiavelli, M. Cromaz, P. Fallon, G. J. Lane, W. Gast, R. M. Lieder, G. Falconi, A. V. Afanasjev, and I. Ragnarsson, Phys. Rev. C **61**, 011305(R) (2000).
- [17] C. M. Petrache, R. Wyss, Zs. Podolyák, D. Bazzacco, G. de Angelis, D. de Acuña, M. De Poli, A. Dewald, E. Farnea, J. Gableske, A. Gadea, S. Lunardi, D. R. Napoli, M. N. Rao, C. Rossi Alvarez, T. Scanferla, C. A. Ur, R. Venturelli, P. von Brentano, and L. H. Zhu, Phys. Rev. C **57**, R10 (1998).
- [18] C. M. Petrache, M. N. Rao, N. H. Medina, R. V. Ribas, D. Bazzacco, S. Lunardi, C. Rossi Alvarez, R. Venturelli, R. Burch, P. Pavan, G. de Angelis, M. De Poli, G. Vedovato, L. H. Zhu, and R. Wyss, Phys. Lett. **B383**, 145 (1996).
- [19] F. G. Kondev, M. A. Riley, D. J. Hartley, T. B. Brown, R. W. Laird, M. Lively, J. Pfohl, R. K. Sheline, E. S. Paul, D. T. Joss, P. J. Nolan, S. L. Shepherd, R. M. Clark, P. Fallon, D. G. Sarantites, M. Devlin, D. R. LaFosse, F. Lerma, R. Wadsworth, I. M. Hibbert, N. J. O'Brien, J. Simpson, and D. E. Archer, Phys. Rev. C **60**, 011303(R) (1999).
- [20] A. Neußer, H. Hübel, A. Al-Khatib, P. Bringel, A. Bürger, N. Nenoff, G. Schönwaßer, A. K. Singh, C. M. Petrache, G. Lo Bianco, I. Ragnarsson, G. B. Hagemann, B. Herskind, D. R. Jensen, G. Sletten, P. Fallon, A. Görgen, P. Bednarczyk, D. Curien, G. Gangopadhyay, A. Korichi, A. Lopez-Martens, B. V. T. Rao, T. S. Reddy, and N. Singh, Phys. Rev. C **70**, 064315 (2004).
- [21] M. A. Bentley, G. C. Ball, H. W. Cranmer-Gordon, P. D. Forsyth, D. Howe, A. R. Mokhtar, J. D. Morrison, J. F. Sharpey-Schafer, P. J. Twin, B. Fant, C. A. Kalfas, A. H. Nelson, J. Simpson, and G. Sletten, Phys. Rev. Lett. **59**, 2141 (1987).
- [22] H. Savajols, A. Korichi, D. Ward, D. Appelbe, G. C. Ball, C. Beausang, F. A. Beck, T. Byrski, D. Curien, P. Dagnall, G. de France, D. Disdier, G. Duchêne, S. Erturk, C. Finck, S. Flibotte, B. Gall, A. Galindo-Uribarri, B. Haas, G. Hackman, V. P. Janzen, B. Kharraja, J. C. Lisle, J. C. Merdinger, S. M. Mullins, S. Pilotte, D. Prévost, D. C. Radford, V. Rauch, C. Rigollet, D. Smalley, M. B. Smith, O. Stezowski, J. Styczen, Ch. Theisen, P. J. Twin, J. P. Vivien, J. C. Waddington, K. Zuber, and I. Ragnarsson, Phys. Rev. Lett. **76**, 4480 (1996).
- [23] R. M. Clark, I. Y. Lee, P. Fallon, D. T. Joss, S. J. Asztalos, J. A. Becker, L. Bernstein, B. Cederwall, M. A. Deleplanque, R. M. Diamond, L. P. Farris, K. Hauschild, W. H. Kelly, A. O. Macchiavelli, P. J. Nolan, N. O'Brien, A. T. Semple, F. S. Stephens, and R. Wadsworth, Phys. Rev. Lett. **76**, 3510 (1996).
- [24] K. Hauschild, R. Wadsworth, I.-Y. Lee, R. M. Clark, P. Fallon, D. B. Fossan, I. M. Hibbert, A. O. Macchiavelli, P. J. Nolan, H. Schnare, A. T. Semple, I. Thorslund, and L. Walker, Phys. Rev. C **52**, R2281 (1995).
- [25] E. Gülmez, H. Li, and J. A. Cizewski, Phys. Rev. C **36**, 2371 (1987).
- [26] J. Simpson, Z. Phys. A **358**, 139 (1997); F. A. Beck, Prog. Part. Nucl. Phys. **28**, 443 (1992).
- [27] D. C. Radford, Nucl. Instrum. Methods Phys. Res. A **361**, 297 (1995).
- [28] L. K. Peker, Nucl. Data Sheets **26**, 473 (1979).
- [29] J. C. Merdinger, F. A. Beck, E. Bozek, T. Byrski, C. Gehringer, Y. Schutz, and J. P. Vivien, Nucl. Phys. **A346**, 281 (1980).
- [30] J. C. Merdinger, Phys. Scr. **24**, 249 (1981).
- [31] T. Bengtsson and I. Ragnarsson, Nucl. Phys. **A436**, 14 (1985).
- [32] A. O. Evans *et al.*, Phys. Rev. Lett. **92**, 252502 (2004).